PAPER

Check for updates

Optimization of magnetic nanoparticles for engineering erythrocytes as theranostic agents†

Laura Maria Slavu, [ID] ‡[a] Antonella Antonelli, [ID] *‡[b] Emanuele Salvatore Scarpa,[b] Pasant Abdalla,[b] Claire Wilhelm,[c] Niccolò Silvestri,[d] Teresa Pellegrino, [ID] [d] Konrad Scheffler, [ID] [e] Mauro Magnani,[b] Rosaria Rinaldi*[a,f,g] and Riccardo Di Corato [ID] *[g,h]

The application of superparamagnetic iron oxide nanoparticles (SPIONs) in drug delivery, magnetic resonance imaging, cell tracking, and hyperthermia has been long exploited regarding their inducible magnetic properties. Nevertheless, SPIONs remain rapidly cleared from the circulation by the reticuloendothelial system (RES) or mononuclear phagocyte system, with uptake dependent on several factors such as the hydrodynamic diameter, electrical charge and surface coating. This rapid clearance of SPION-based theranostic agents from circulation is one of the main challenges hampering the medical applications that differ from RES targeting. This work proposes a strategy to render biocompatible SPIONs through their encapsulation in the red blood cells (RBCs). In this work, the research has been focused on the multi-step optimization of chemical synthesis of magnetic nanoparticles (MNPs), precisely iron oxide nanoparticles (IONPs) and zinc manganese-ferrite nanoparticles (Zn/Mn FNPs), for encapsulation in human and murine RBCs. The encapsulation through the transient opening of RBC membrane pores requires extensive efforts to deliver high-quality nanoparticles in terms of chemical properties, morphology, stability and biocompatibility. After reaching this goal, *in vitro* experiments were performed with selected nanomaterials to investigate the potential of engineered MNP-RBC constructs in theranostic approaches.

1. Introduction

In the last few years, different nanoscale materials with unique physiochemical properties have led to obtaining innovative nanoparticle-based technologies that offer exciting approaches to disease diagnostics and therapeutics. The literature abun-

[a]*Mathematics and Physics "E. De Giorgi" Department, University of Salento, Via Monteroni, Lecce 73100, Italy. E-mail: ross.rinaldi@unisalento.it*
[b]*Dipartimento di Scienze Biomolecolari, Università degli Studi di Urbino Carlo Bo, Via Saffi 2, Urbino 61029, Italy. E-mail: antonella.antonelli@uniurb.it*
[c]*Laboratoire Physico Chimie Curie, UMR 168, CNRS, Institut Curie, PSL University, Sorbonne Université, 75005 Paris, France*
[d]*Italian Institute of Technology, via Morego 30, 16131 Genoa, Italy*
[e]*Section for Biomedical Imaging, University Medical Center Hamburg-Eppendorf, 22529 Hamburg, Germany*
[f]*Scuola Superiore ISUFI, University of Salento, Via Monteroni, University Campus, Lecce 73100, Italy*
[g]*Institute for Microelectronics and Microsystems (IMM), CNR, Via Monteroni, Lecce 73100, Italy. E-mail: riccardo.dicorato@cnr.it*
[h]*Center for Biomolecular Nanotechnologies, Istituto Italiano di Tecnologia, Arnesano 73010, Italy*
†Electronic supplementary information (ESI) available. See DOI: https://doi.org/10.1039/d3bm00264k
‡These authors contributed equally to this work.

dantly reports the optimization of the size, shape and/or surface chemistry of the nanoparticles to allow their functionalities to be tailored for different biomedical applications. Nanoparticles, such as SPIONs, used to enhance the contrast of an imaging modality also have size-dependent properties and the nanoparticle size also influences image contrast, cellular uptake and tumor permeability.[1] The rapid clearance of nanoparticles from the blood stream by the RES represents an obstacle to ensuring that contrast agents can achieve the required accumulation in the target tissue.[2,3] On the other hand, the macrophages of RES with their scavenger receptors represent a very efficient system for recognizing a broad spectrum of surface modification and coating of large and small nanoparticles. Given the preferential uptake of SPIONs by the liver, the RES is exploited for MRI, because it reveals liver tumor deposits as negative images.[4,5] In the last few decades, numerous efforts have been made in order to develop original diagnostic and treatment methods for different diseases based on the use of drug delivery systems (such as liposomes, nanoparticles, micelles, and dendrimers) with which it is possible to protect the loaded drug against premature degradation in the body, improving its bioavailability, or/and to increase the therapeutic agent at its site of action.[6,7] However, to date, the

number of these nanodevices that have reached commercialization after a successful clinical trial remains extremely low, mostly due to long and challenging regulatory pathways.[8] Moreover, innovative materials need to be considered since they can represent important barriers that limit the clinical development of nanoparticles for drug delivery purposes and industrial scale-up.

In this way, the chemical formulation of nanoparticles with a compound without a regulatory status (*i.e.* excipients, organic solvents, new synthetic polymers, *etc.*) makes the development process more challenging, longer and, therefore, more expensive.[9] The complexity and reproducibility of the preparative method of nanoparticles are also important aspects that must be considered since they could hinder the continuity of the project towards clinical phases.

The current development in medical imaging technology aims for early diagnosis and consequently, timely and personalized treatment of the pathology, which often implies the visualization of specific targets in the diseased organism by labeling with tracer agents such as magnetic iron oxide nanoparticles that have been extensively explored especially as magnetic resonance imaging (MRI) tracers through control over their size, composition and morphology.[10] Although advances in nanotechnology have improved the stability and biocompatibility of iron oxide-based contrast agents, the phagocytic system still limits the applicability of these tracers that have a blood half-life range of 1–3 h and the time window for bolus-based measurements is only a few minutes.[11] Moreover, several iron oxide contrast agents were discontinued due to safety concerns.[12]

In the last few years, a strategy has been developed based on the encapsulation of some SPIONs, mainly commercial, and/or USPION contrast agents in red blood cells (RBCs) as a useful alternative to overcome the limitations described above.[13] When placed in a hypotonic solution, human erythrocytes have a remarkable capacity to undergo reversible membrane swelling with the simultaneous appearance of pores large enough to be crossed by metabolites and macromolecules; this property has been carefully investigated for a long time in laboratories, and resealed erythrocytes have been proposed as carriers and bio-reactors suitable for use in the treatment of various diseases.[14,15] In fact, RBCs have potential to act as biocompatible carriers for several compounds[16–20] and contrast agents since they survive in circulation for weeks, therefore permitting a potential extension of the time window for imaging in diagnostic applications. In the last few years, some efforts have been made to identify, among commercially available and preclinical SPIONs, those that are efficiently encapsulated in RBCs.[21] Indeed, not all iron oxide nanoparticles can be efficiently loaded into RBCs and their encapsulation varies according to several factors, namely the synthesis protocol, the dispersant agent and the nanoparticle size. Moreover, if SPIONs are not stabilized properly, the particle suspensions may aggregate or the particle core and coating may degrade. Hence, to be able to use RBCs as an effective diagnostic tool in this field, there is an urgent need to identify magnetic nanomaterials that are potentially suitable for producing SPION-loaded RBCs with long half-lives in blood circulation. Such SPION-loaded RBCs could open up a variety of medical applications that require intravascular magnetic tracers.

In this work we focused our attention on the possibility to encapsulate newly synthesized magnetic nanoparticles (MNPs) with different chemico-physical characteristics, into human RBCs through the open membrane pores without affecting cell viability. The main challenge in producing nanoparticles for the engineering of RBCs is represented by the pathway of the material internalization: unlike other mammalian cells (that take up many kinds of nanomaterials with different shapes and sizes by a well-defined mechanism of endocytosis or phagocytosis[22,23]), the nanoparticle loading into RBCs is only related to the passage through transient opened pores on the cell membrane. Consequently, the morphology, monodispersity and stability of the nanomaterial become critical aspects for the encapsulation of SPIONs in RBCs. The immediate perspective of this work is optimization of the stability of the nanoparticle suspensions for enhancing the encapsulation rate into the RBCs with the future perspective of characterizing their magnetic behavior in related applications. For example, SPION-RBC constructs could represent new intravascular contrast agents for some diagnostic applications, such as MRI/fMRI and magnetic particle imaging (MPI).[24]

In order to obtain high quality SPIONs, there are several specific parameters to set, which must be strictly followed in order to tailor the magnetic properties to the aimed application and gain maximum efficiency and no side effects in humans.[25,26] Herein, the preparation of different MNPs based on iron oxide or zinc manganese-ferrite nanoparticles is described. Synthetic strategies such as the thermal decomposition route are still not ideal to achieve highly loaded RBCs since these nanoparticles need an additional processing to be transferred in water,[27] with a low-yield in terms of the final concentration. Therefore, the strategy here was to optimize the well-established co-precipitation method, and reach a high yield of concentrated nanoparticles and further RBC loading.[28,29] Temperature, nucleation and growth time, filtration, and coating were finely adjusted to deliver the most suitable nanomaterials for encapsulation in the RBCs. The biological parameters of the selected best engineered MNP-RBC constructs as well as the efficiency of magnetic nanoparticle encapsulation and their potential as magnetic carriers eligible for theranostic applications were evaluated.

2. Experimental section

2.1 Materials

All solvents were of analytical grade and used with no modifications. Fe(III) chloride hexahydrate, Fe(II) chloride tetrahydrate, Mn(II) chloride tetrahydrate, Zn(II) chloride, trisodium citrate dihydrate, ammonium hydroxide and epoxy resin kit were purchased from Sigma-Aldrich. Dextran (70 kDa) was purchased from Carl Roth. Ultrapure water produced with a

Smart2Pure 12 system (Thermo Scientific) was used throughout all experiments.

2.2 Synthesis of magnetic nanoparticles

A series of syntheses were performed by the co-precipitation method to produce iron oxide nanoparticles and zinc manganese ferrite nanoparticles. Different parameters were modified and studied in order to analyse their effect on the resulting nanoparticles. For the synthesis of iron oxide nanoparticles, a standard protocol used for the preparation of Resovist®-like nanoparticles has been modified.[30] In detail, 318 mg of $FeCl_2$ (1.6 mmol) and 751 mg of $FeCl_3$ (2.8 mmol) were completely dissolved in 10 mL of ultrapure water in a 40 mL glass vial and the resultant solution was warmed to 40 °C using a heating plate, within a time-lapse of 5 minutes. After that, the reaction was carried out by precipitating the iron salts with hydroxide ammonium (NH_4OH) under vigorous stirring, maintaining the temperature at 40 °C. In detail, 10 mL of hydroxide ammonium (7.5%, in water) were added to the iron salt solution, by using a syringe pump with a flow rate of 5 mL min^{-1} under magnetic stirring. During the nucleation process, black precipitates were obtained as uncoated iron oxide nanoparticles. After 3 hours of reaction at 40 °C, the as-synthesized nanoparticles were washed 5 times with water by magnetic decantation using a magnet of 0.3 T and resuspended in 10 mL of water for subsequent stabilization steps. All the different parameters modified in the preparation of the nanoparticles (including doping with Zn and Mn for the preparation of Zn/Mn FNPs) are reported in the tables in the Results section. In particular, the reaction step subsequent to the base addition (3 hours in the above-described protocol) was reduced to 1–5 minutes; more details are provided in the Results section in section 3.6.

2.3 Citrate coating

The synthesized nude nanoparticles (*i.e.* without any capping agent) were not stable in aqueous suspension. To enhance their stability, a layer of sodium citrate was grafted onto the nanoparticle surface. 20 mL of sodium citrate solution (2 M, in water) were added to the nanoparticles (10 mL) and the suspension was heated at 80 °C under vigorous stirring for 1 hour on the heating plate. Soon after, the suspension was ultrasonicated (using an ultrasonic homogenizer Bandelin HD3100) for 30 min at 20 kHz, at the maximum power output. Immediately after that, the nanoparticles were washed by magnetic decantation after acetone addition (5 times) and finally resuspended in 5 mL of sodium citrate (5 mM water, as stabilizer buffer for storage). The suspension was then placed for 20 min in an ultrasound bath (56 kHz) at 60 °C to facilitate the evaporation of any trace of acetone. Finally, the sample was filtered by using a nylon syringe filter, with a pore size of 0.4 μm, to remove any possible large aggregate in the suspension.

2.4 Dextran coating

In order to enhance the biocompatibility and colloidal stability of the nanoparticles, a ligand exchange strategy was applied, where the citrate coating was replaced by a layer of non-modi-fied dextran (molecular weight: 70 kDa). 10 mL of a dextran solution (280 mM, in water) were added to 5 mL of citrate-coated magnetic nanoparticles and mixed using the heating plate for 30 minutes at 70 °C. As for the previous coating step, the sample was first immersed in a bath sonicator for 15 min (at 60 °C) and immediately ultrasonicated (with an ultrasound homogenizer) for another 30 min. Soon after, the suspension was filtered with 0.22 and 0.1 μm nylon syringe filters and centrifuged at 2500g with a concentrator tube (100 kDa MWCO, Sartorius) in order to remove the excess of dextran and citrate molecules, applying five complete washing steps. Finally, the concentrated sample was resuspended in 2 mL of ultrapure water for characterization and encapsulation into human and murine RBCs.

2.5 Encapsulation of SPIONs in RBCs

Human blood was collected from healthy volunteers into heparinized tubes. RBCs were isolated by centrifugation at 1400g at 4 °C for 10 min from freshly drawn blood. The serum and buffy coat were removed and the packed cells were washed three times with Hepes buffer (10 mM Hepes, 140 mM NaCl, 5 mM glucose, pH 7.4) and then resuspended in the same buffer with 70% hematocrit. These cells were dialyzed in the presence of magnetic nanoparticles for 75 min using a tube with a 12–14 kDa cut-off in 50 vol of a dialysis buffer (10 mM $NaHCO_3$, 10 mM NaH_2PO_4, 20 mM glucose, and 4 mM $MgCl_2$ at pH 7.4), containing 2 mM ATP and 3 mM reduced gluta-thione. The osmolarity of the dialysis buffer was 70 mOsm. All these procedures were performed a 4 °C under sterile conditions. Resealing of RBCs was achieved by adding 0.1 vol of PIGPA (5 mM adenine, 100 mM inosine, 2 mM ATP, 100 mM glucose, 100 mM sodium pyruvate, 4 mM $MgCl_2$, 194 mM NaCl, 1.606 M KCl, and 35 mM NaH_2PO_4 at pH 7.4) per vol of dialyzed RBCs and by incubating at 37 °C for 45 min. The resealed cells were recovered by centrifugation at 400g and washed four times with Hepes buffer to remove the untrapped magnetic nanomaterial. Erythrocytes were loaded using different amounts of nanoparticles (from 2.8 mg Fe to 22.4 mg Fe per mL RBCs 70% Ht) to produce L1–L4 loaded RBCs. Following the same procedure, unloaded erythrocytes (unloaded-RBCs) were prepared, with the exception that they were dialyzed in the absence of the magnetic material. The encapsulation of magnetic nanoparticles in murine RBCs was performed by using the same procedure of hypotonic dialysis, isotonic resealing and reannealing with a few modifications. In particular, the murine blood withdrawn from ocular artery was centrifuged at 400g and the dialysis buffer was 88 mOsm. The magnetic susceptibility of the selected SPION-loaded RBCs and some biological parameters such as the mean corpuscular volume (MCV), mean hemoglobin concentration (MCH) and mean corpuscular hemoglobin concentration (MCHC) were examined to evaluate cell integrity as reported in ref. 19 and 21.

2.6 Ethical conduct of research

The authors state that they have obtained appropriate institutional review board approval or have followed the principles

outlined in the Declaration of Helsinki for all human experimental investigations. In addition, for investigations using human blood, informed consent has been obtained from the participants involved, on the basis of an official document of accordance with the Transfusion Center of "S. Maria della Misericordia" Hospital in Urbino (PU), Italy. The experiments with murine blood were performed based on "Ethics statement". Housing and blood withdrawal from ICR(CD1) mice were in accordance with the recommendations in the Guide for the Care and Use of Laboratory Animals by the Health Ministry, D.lgs. 26/2014 (endorsement number 287/2022-PR).

2.7 Transmission electron microscopy

The morphology and distribution of the magnetic nanoparticles (MNPs) were studied using a transmission electron microscope (TEM) JEOL JEM-1011 operating at an accelerating voltage of 100 kV. The nanoparticles were prepared by dropping a few microliters of nanoparticles onto a formvar-coated copper grid. All the reported images of free MNPs have been acquired with grids prepared just after the completion of the synthesis process, diluting a few microliters of high-concentration final suspensions in proper buffer or water according to the surface coating. TEM analysis on RBC samples was performed after their fixation with 2.5% glutaraldehyde as previously reported.[21] Unloaded and SPION-loaded RBCs were investigated by two methods: for the analysis of the whole-RBC, 5 μL of glutaraldehyde-fixed RBCs (1–4% Ht) were dropped onto a formvar-coated copper grid (placed on a parafilm) and left to react for 5 minutes; after that, the grid was washed twice upside down on a 50 μL drop of water, for 1 minute; then, the grid was positioned again on a 50 μL drop of cold carboxymethyl-dextran (10 mg mL^{-1}, in water) for 10 minutes; finally the excess of liquid was removed for capillarity with a Whatman filter paper (type 1). For the analysis of RBC slices, glutaraldehyde-fixed cells were then post-fixed in 1% OsO_4, dehydrated with ethanol and embedded in epoxy resin. Thin sections of 80 nm were obtained using an ultramicrotome and collected onto copper TEM grids.

2.8 Magnetic particle spectroscopy (MPS) analysis

MPS can be used to measure the response of particles by applying a sinusoidal magnetic field. MPS analyses of 10 μL of selected MNPs and MNP-loaded RBCs were performed and compared to bulk- and immobilized-MNPs, at the same concentration as reported in ref. 31. The MPS signal was acquired upon application of a sinusoidal magnetic field with an amplitude of 20 mT peak-to-peak and a base frequency of 26.042 kHz as described in ref. 21. The decay of the spectral response over the higher harmonics characterizes the intrinsic dynamic re-magnetization properties of superparamagnetic nanoparticles in tracer samples. To compare the different particle responses with each other, the measured MPS results were scaled to the lowest concentration of all probes (1.46 mmol L^{-1}). The particles' MPS results are verified against a measurement of unloaded RBCs as well as an empty measurement.

Thus, the results are valid up to the frequency where their response crosses the response of the reference signal.

2.9 Dynamic light scattering (DLS)

DLS was performed on an aqueous ferrofluid with a Malvern Zetasizer Nano ZSP, equipped with a He–Ne laser (λ = 633 nm, max 5 mW) and operating at a scattering angle of 173°. In all analysis 1 mL of MNP suspensions were placed in a 4.5 mL polystyrene cuvette.

2.10 Elemental analysis

The metal concentrations were measured by elemental analysis, using an inductively coupled plasma atomic emission spectrometer (Varian 720 ICP-OES). Before analysis, the samples were digested in a concentrated HCl/HNO$_3$ 3 : 1 (v/v) solution.

2.11 Fourier transform infrared spectroscopy (FTIR)

IR spectra were acquired using a JASCO FT/IR6800 spectrometer, equipped with a diamond ATR module. Spectral manipulations were performed using the spectral analysis software from Jasco. Spectra were acquired in the range of 4000–400 cm^{-1} at room temperature on dried samples.

2.12 Superconducting quantum interference device (SQUID)

Magnetic measurements were performed on a SQUID system from Quantum Design Inc. Hysteresis loops were recorded within a magnetic field of ±5584 kA m^{-1} at 5 K and 298 K. Samples were prepared by dispersing 50 μL of solution (ca. 1 g L^{-1}) in gypsum powder (50 mg), in order to obtain a solid paste suitable for the analysis. Magnetization curves were normalized by the metal content (Fe or Fe + Zn + Mn) obtained by ICP-OES.

2.13 Hyperthermia characterization

Photothermia and magnetic hyperthermia were implemented to evaluate the MNPs' potential as heating agents. Concerning photothermia, the heating efficiency of MNPs was measured with a laser at 808 nm (infrared first biological window). The temperature of the sample was recorded with an infrared thermal camera (FLIR SC7000), operating at 1 frame per second, and controlled with the proprietary software ALTAIR. The nanoparticle suspensions were irradiated at a distance of 4 cm, from the center of the sample with a laser power density of 1.6 W cm^{-2} for 10 min and represented by the temperature elevation curve recorded with an IR camera. The heating effect for each sample was measured using a 0.5 mL tube containing a volume of 50 μL of aqueous suspension, as a function of iron concentrations ranging from 2.5 to 200 mM, with increasing steps of 4-fold. To confirm the increment of the temperature, the measurement was repeated 2 times for each sample. Control measurement of pure water revealed a temperature increase below 2 °C under 10 min laser irradiation. Regarding the magnetic hyperthermia, the experiments were carried out using similar 0.5 mL Eppendorf tubes containing 50 μL of the MNP suspensions, excited for 10 min by an alternating mag-

netic field generator device (DM3, NanoScale Biomagnetics) operating at 18 mT with a frequency of 471 kHz. The temperature curves were acquired with the same thermal camera reported above. Both the hyperthermia protocols (parameters, exposure, and timing) have been validated in previous studies.[32,33]

2.14 Magnetic resonance imaging (MRI)

Magnetic resonance imaging was performed using a pre-clinical 1 Tesla desktop MRI scanner (Bruker ICON). All samples were imaged with a T_2 multislice multiecho (MSME) sequence with a TR of 3000 ms, multiple TE from 12 to 90 ms, and a flip angle of 180°. For the preparation of phantoms, sequential concentrations of MNPs or MNPs-RBCs were dispersed in 0.5% agarose (at 37 °C) and immediately cooled (4 °C) for avoiding the sedimentation of the RBCs in the tube.

3. Results and discussion

For the synthesis of SPIONs, a standard co-precipitation method was considered as the starting point. The aim was to determine the most influential parameters, in order to tune the desired properties of morphology, particle size distribution, monodispersity, composition and surface properties to facilitate encapsulation into the red blood cells as the final goal. All the variations to the standard protocol described above (Experimental section) are reported below, focusing on specific conditions.

3.1 Optimization of iron oxide nanoparticles: temperature effect

The temperature is an important parameter when synthesizing magnetic nanoparticles, since it has a direct impact on the crystal size. In the previous studies concerning aqueous synthesis by precipitation, the temperature used was very variable, ranging from the room temperature, also reported in the first pioneering study on the method,[29] to values close to the boiling point of water.[34,35] Herein, three different series of nanoparticles were obtained by varying the temperature of the precursor solutions. A first batch of citrate-coated IONPs has been synthesized at temperature intervals from 25 °C to 60 °C, for evaluating the resulting size and shape (Table S1,† MNPs 1–4). Initially, the salt solution was kept at a constant temperature (25 °C), whereas the base (NH4OH) was added at different temperatures, ranging from 25 °C to 60 °C. It was observed that the increase of the NH4OH solution temperature tends to generate a progressive aggregation of the resulting nanoparticles; DLS analysis confirmed the observed trend, with a high degree of polydispersity (PDI) measured for all the samples.

For the preparation of the second series of samples, both the salt solution and ammonium hydroxide were maintained at the same temperatures (MNPs 5–7). This approach leads to the non-controlled formation of some clusters during the reaction, as can be seen from DLS measurements, which implies a slight polydispersity. These nanoparticles were much larger, less uniform and more aggregated than typical spherical nanoparticles, with a similar size trend compared to the first batch. Finally, with the third series of nanoparticles (MNPs 8–10) the ammonium hydroxide was kept at room temperature whereas the temperature of the saline solution was tuned. The effect of the temperature was confirmed, observing a reduction of particle size correlated with the increase of the reaction temperature. The crystal size is reduced when the temperature is blocked at 40 °C (MNPs 9); nanoparticles show a good hydrodynamic size distribution (25–35 nm by DLS analysis) when the salt solution was heated to 40 °C and the ammonium hydroxide (NH4OH) was kept at 25 °C. TEM measurements showed an average core diameter between 7 nm and 12 nm (Fig. 1).

3.2 Citrate coating effect

The colloidal stability of coated MNPs was evaluated for nanoparticles stabilized using three distinct concentrations of sodium citrate: 0.5, 1 and 2 M. To decipher the stability of the citrate coated NPs, macroscopically the colloidal stability of the suspensions was initially monitored. Each sample was left in a glass vial under observation, for 1 week, in order to see if the nanoparticles were precipitating, even partially, during this period. The sample coated with the 0.5 M citrate solution precipitated after 24 hours, whereas the sample obtained with the 1 M solution started to sediment after 3 days. The most suitable sample was prepared using the 2 M sodium citrate solution, which did not present any precipitation and remained stable even over a period of 6 months. TEM and DLS analyses of this sample (MNPs 13, Fig. 2 and Table S2†) showed an
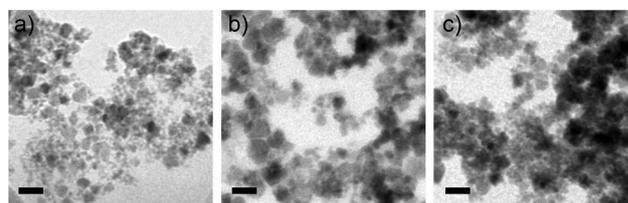

Fig. 1 TEM images of sample MNPs 3 (a), MNPs 6 (b) and MNPs 9 (c), obtained by varying the temperature of the precursor solutions. All scale bars correspond to 20 nm.
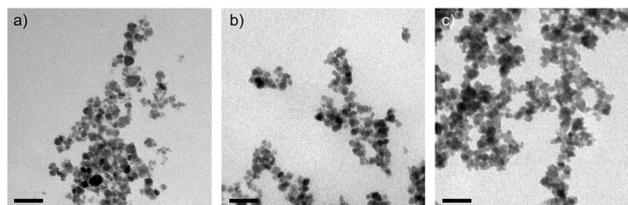

Fig. 2 TEM images of the citrate-coated iron oxide MNPs obtained with different concentrations of sodium citrate solution: (a) MNPs 11 (0.5 M); (b) MNPs 12 (1 M) and (c) MNPs 13 (2 M). All scale bars correspond to 50 nm.

enhanced size distribution and a quite small PDI in comparison with the other samples where some aggregations were observed. Unfortunately, despite the high concentration, monodispersibility, colloidal stability and filtration (see section 3.5) of the magnetic nanoparticle suspensions, the morphology analyses evidenced the formation of some small iron oxide clusters (below 100 nm) which could invalidate the encapsulation procedure through the transient pore of RBCs.

3.3 Dextran coating effect

Dextran is a valuable alternative molecule for the coating of MNPs, being a biocompatible, biodegradable, and water-soluble polymer. To enhance the biocompatibility and colloidal stability of MNPs, the citrate molecules at the surface were substituted with a thin layer of the polysaccharide. The ligand exchange procedure was carried out using as starting particles the MNPs 13 described above. Different amounts of dextran were evaluated for assessing the most suitable conditions in terms of size and stability (Table 1). A high amount of the polysaccharide (MNPs 14–15) resulted in very stable suspensions, but with a large hydrodynamic diameter, above 100 nm. By reducing the quantity of dextran used in the procedure, the resulting hydrodynamic diameter was controlled between 34 and 74 nm. Below a concentration threshold (MNPs 22), the dextran used in the exchange procedure was not suitable to guarantee a proper stability. Considering the morphology and the distribution of all the dextran-coated MNPs, the sample MNPs 20 (Fig. 3a and b), obtained with an overall amount of 2.8 mmol of polysaccharide (corresponding to a final dextran concentration of 187 mM), was considered the best formulation within this experimental set.

The dextran molarity has been calculated with the final reaction volume of 15 mL and considering the molecular weight of the glucose monomer (180.16 Da).

FT-IR measurements were performed on prepared nanoparticles to assess the presence of the different coatings (Fig. 3c). The ATR spectra of sodium citrate and dextran were acquired directly by analyzing the commercial powders. The characteristic bands of COO^- at 1583 cm^{-1} (antisymmetric stretching) and 1417 cm^{-1} (symmetric stretching) were detected for sodium citrate; both bands were revealed in the citrate-coated MNPs, with a red shift of the symmetric stretching to 1396 cm^{-1}. Concerning the dextran, two main func-
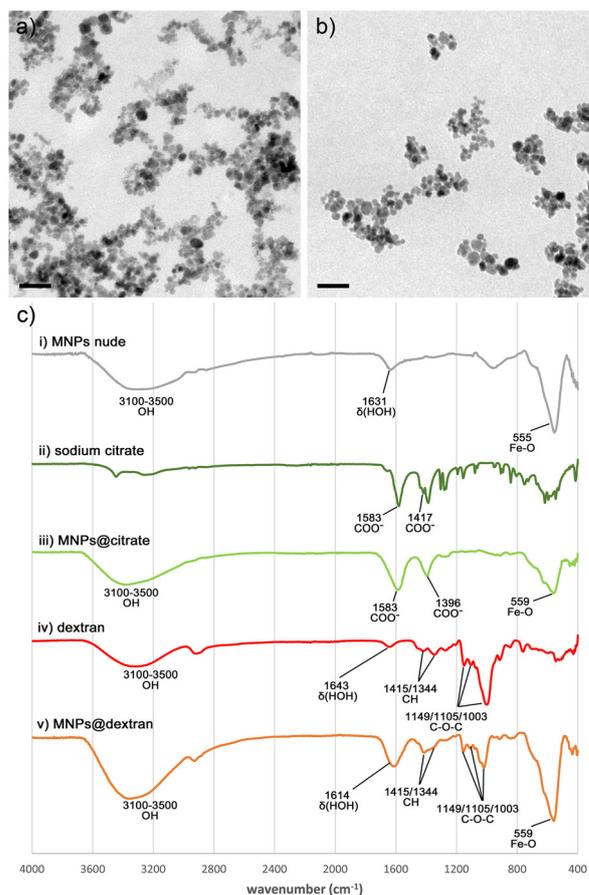

Fig. 3 TEM images of dextran-coated MNPs 20. Panel (a) shows a non-filtered MNP preparation, whereas panel (b) shows 0.1 μm filtered MNPs 20. The filtration step was added to remove any possible aggregate from the suspension. All scale bars correspond to 50 nm: (c) ATR-FTIR spectra of (i) nude MNPs, (ii) sodium citrate, (iii) citrate-coated MNPs, (iv) dextran and (v) dextran-coated MNPs.

tional groups were detected: the stretching vibration of C–O–C (at 1149, 1105 and 1003 cm^{-1}) and the vibration modes related to υ(C–H) (at 1415 and 1344 cm^{-1}); the same characteristic peaks were revealed in the dextran-coated MNPs. In this sample, the peaks related to citrate molecules were not detected at all, confirming the ligand exchange procedure at the surface of the nanoparticles. In all the MNP-spectra a peak at 555–560 cm^{-1} was observed, related to the Fe–O bond. Moreover, in all the spectra (except sodium citrate) a large shoulder between 3100 and 3500 cm^{-1} was observed for the stretching of OH. Finally, for nude iron oxide and for both the samples containing dextran, an intense peak in the range 1600–1650 was detected, attributed to the vibration of H–O–H (δO–H) of coordinated water molecules.

3.4 Nucleation rate effect

One of the parameters that could significantly influence the size of the nanoparticles, by using the co-precipitation method, is the rate of MNP nucleation. For this purpose, some samples were synthesized by adding the same volume of

Table 1 List of MNPs coated with different amounts of dextran

Samples	[Dextran] (M)	DLS size (nm)	PDI
MNPs 14	3.7	125.2	0.184
MNPs 15	7.4	107.8	0.168
MNPs 16	3	61.45	0.156
MNPs 17	1.5	67.84	0.223
MNPs 18	0.75	74.07	0.139
MNPs 19	0.375	65.06	0.213
MNPs 20	**0.187**	**34.04**	**0.214**
MNPs 21	0.093	58.05	0.392
MNPs 22	0.047	104.9	0.316

ammonium hydroxide by flow injection at different time intervals, using a controlled syringe pump. The formation of the MNPs starts as soon as the first drops of ammonium hydroxide are added to the iron salt solution. The interval time for each sample is reported in Table S3† (MNPs 23–27). From TEM analysis, the best morphology was observed for the MNPs obtained with nucleation intervals of 2 and 4 min (MNPs 25–26, Fig. S1†). Regarding the other reaction times (30″, 1′, and 10′), unfortunately, the nucleation time was too fast or too slow, resulting in non-controlled nucleation and an unstable cloudy suspension. This set of trials confirmed the 2-minute addition rate of the standard protocol as the best condition.

3.5 Filtration of MNPs

As anticipated in Fig. 3, in order to minimize the presence of any aggregate in the nanoparticle suspension, multiple filtrations were introduced, with filter pore sizes ranging from 0.44 μm to 0.1 μm. The filtration was achieved through a multi-step protocol: the first filtration was performed with a filter pore size of 0.44 μm on the citrate-coated nanoparticles; then, the second one was carried out with a filter pore size of 0.22 μm on the dextran-coated nanoparticles followed by the third filtration with a 0.1 μm pore size on the final high-concentration sample, recovered from the centrifugal concentrator tubes. A significant improvement in the overall quality of the suspensions has been observed, in terms of colloidal stability and polydispersity. It is noteworthy to mention that the proposed synthesis does not consider magnetic sorting to separate different size populations within the same preparation; a small presence of aggregates, even if consisting of a few nanoparticles, must be considered and could represent a limitation in the loading procedure into RBCs. Therefore, the use of a 0.1 μm filter helped remove also the smallest aggregates, which eluded the bigger filters (0.22 or 0.44 μm cut-off) or the sedimentation by low-speed centrifugation. Considering the iron amount used for the synthesis (*i.e.* 245 mg of Fe) and the average final concentration of filtered MNPs (>0.5 M in terms of Fe, for 5 mL of suspension, measured by ICP-OES, as described in the Experimental section), the overall yield of the synthesis is higher than 60%, confirming that the total loss (not only referring to the three filtrations) is not so pronounced.

3.6 Growth phase effect

The crystal growth was monitored as the last parameter for the optimization of the iron oxide nanoparticles. The main aim was to reduce the crystal size, and therefore to achieve a reduction of the overall size of the nanoparticles. It is noteworthy to mention that all the previously reported formulations (from MNP-1 to MNP-27) were synthesized by applying a growing step of 3 hours, to be considered from the end of the base addition. Here, 1 mL of a 2 M citric acid solution was used to stop the growth of the nanoparticles at different time lapses after the addition of ammonium hydroxide. The addition of the acidic solution altered the alkaline environment suitable for the growth of the nanoparticles; moreover, although the nanoparticles were immediately washed (five

times by water) by magnetic decantation after citric acid addition, some molecules were grafted onto the MNP nude surface. The preparation conditions of each sample are reported in Table 2.

For a comparison between the different suspensions of nanoparticles, the sample MNPs 20 was synthesized by using the classic method where no citric acid was used to stop the 3 h-growth step.

The obtained nanoparticles had a smaller and more regular shape than MNPs 20, as measured by TEM analysis observation (Fig. 4). Moreover, the samples obtained at 30 and 60″ showed a narrow hydrodynamic diameter and a very low polydispersity, by DLS analysis. The colloidal stability of such a formulation was excellent, with the absence of any sedimentation for months at room temperature.

3.7 Introducing doping elements: Zn/Mn ferrite nanoparticles

Among the different magnetic materials, doped ferrite nanoparticles are of particular interest because of their moderate magnetocrystalline anisotropy and high saturation of magnetization. In order to modify the magnetic properties of the synthesized MNPs, one of the methods used is tuning the proportion of the chemical elements used. In this direction, Zn/Mn FNPs have been synthesized by introducing the two doping elements within the synthesis protocol set for the iron oxide nanoparticles.

First, to establish the most suitable amount of elements used for the synthesis, different molar ratios between $FeCl_2$, $FeCl_3$, $MnCl_2$ and $ZnCl_2$ were applied. Hence, the amount of $FeCl_3$ (2.8 mmol) was maintained constant, while that of $FeCl_2$ (1.6 mmol) was reduced to 0.8 mmol. This means that the other 0.8 mmol of XCl_2 salt (where X is Zn or Mn) was replaced with different amounts of zinc and/or manganese (Table 3). The chemical analysis was performed using inductively

Table 2 List of iron oxide MNPs obtained by reducing the crystal growth step time

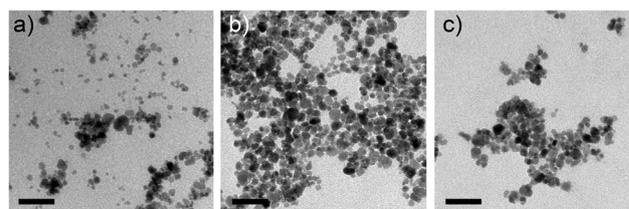| Samples	Crystal growth	[Fe] (mM)	DLS size (nm)	PDI
MNPs 28	30 s	996.9	40.34	0.127
MNPs 29	**60 s**	**881.0**	**34.43**	**0.158**
MNPs 30	120 s	652	27.61	0.274
MNPs 31	300 s	1887	43.98	0.268

Fig. 4 TEM images of iron oxide MNPs obtained with crystal growth steps of 30″ (MNPs 28, panel a), 60″ (MNPs 29, panel b) and 120″ (MNPs 30, panel c). All scale bars correspond to 50 nm.

Table 3 List of Zn/Mn FNPs obtained varying the ratio between the metallic ions (Fe, Mn, and Zn) in the synthesis

Samples	MnCl$_2$ (mmol)	ZnCl$_2$ (mmol)	FeCl$_2$ (mmol)	FeCl$_3$ (mmol)	DLS size (nm)	PDI
MNPs 32	0	0	1.6	2.8	45.21	0.168
MNPs 33	0	0.8	0.8	2.8	36.86	0.227
MNPs 34	0.16	0.64	0.8	2.8	92.24	0.401
MNPs 35	0.32	0.48	0.8	2.8	43.19	0.190
MNPs 36	**0.48**	**0.32**	**0.8**	**2.8**	**25.57**	**0.196**
MNPs 37	0.64	0.16	0.8	2.8	38.93	0.346
MNPs 38	0.8	0	0.8	2.8	59.25	0.198

All the reported analyses referred to citrate-coated nanoparticles.

coupled plasma (ICP), which confirmed the elemental composition used for all the samples synthesized.

After an accurate study of the morphology of nanoparticle suspensions, an evident difference was observed between the sample MNPs 36 and the other remaining samples. TEM analysis (Fig. S2†) showed that the sample MNPs 36 presented a more defined and quasi-spherical shape. Regarding the other samples, they were much larger and less uniform than the sample MNPs 36, with some nanoparticles reaching a hydrodynamic diameter of 80–90 nm by DLS, with a higher polydispersity index.

The magnetic properties of the samples MNPs 32–MNPs 38 were systematically investigated by recording the temperature dependent magnetization curves at 298 K and 5 K (Fig. 5). The samples at 298 K are all in the superparamagnetic regime,
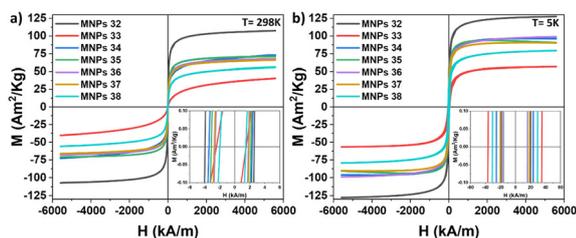
Fig. 5 Magnetization *versus* applied magnetic field curves for Zn/Mn FNPs obtained by varying the ratio between the metallic ions (Fe, Mn, and Zn) in the synthesis. $M–H$ magnetization curves measured at (a) 298 K and (b) 5 K.

showing coercive fields (H_c) smaller than 5.1 kA m^{-1} (Fig. 5a and Table 4). The highest saturation magnetization (M_s) values at 298 K were achieved by the MNPs 32 sample (pure iron oxide) with a value of 107.5 Am^2 kg^{-1}, followed by the samples doped with both Mn and Zn with M_s values between 66 and 73 Am^2 kg^{-1}. The samples doped with only Zn or Mn showed the lowest values of M_s (40.3 e 55.8 Am^2 kg^{-1}, respectively). The magnetization measurements at 5 K showed larger values matching the trend observed at 298 K with also larger coercivity field (H_c), confirming the suitability of these nanoparticles for biological applications.

Considering the results achieved by tuning the growth phase for iron oxide nanoparticles, a similar approach has been tested for Zn/Mn FNPs, by stopping the growth of the crystal core by adding a citric acid solution. Interestingly, a growth time of 60″ (ideal condition for iron oxide) was not sufficient to obtain a stable nanoparticle suspension. Therefore, the reaction time for the ferrites was increased to 90″ (MNPs 39), 120″ (MNPs 40) and 300″ (MNPs 41), as reported in Table 5 and in Fig. 6. The sample MNPs 36$_{DX}$ was obtained by applying a standard 3 hours step of reaction and it was used for comparison with the fast-reaction samples.

3.8 Advanced characterization of MNPs

According to the above-described formulations, an advanced characterization was performed on four samples: two standard samples with a long growth phase (3 hours, MNPs 20 for iron oxide and MNPs 36 for ferrite nanoparticles) and two samples obtained with a short growth phase (MNPs 29 for iron oxide and MNPs 40 for ferrite nanoparticles). According to TEM analysis (Fig. 7a–c), the core size of iron oxide nanoparticles ranged from 5–6 nm to 17–18 nm for both the formulations, but the average size resulted in a reduction of 2 nm for the MNPs 29 (8.8 ± 2 nm) in comparison with the standard MNPs 20 (10.7 ± 2.3 nm). The coefficient of variation (CV) did not change significantly, reducing from 22.5% for MNPs 20 to 21.2% for MNPs 29. A similar trend was observed with the Zn/Mn FNPs, with the mean size shifting from 7.5 ± 1.5 nm of MNPs 36 to a smaller value of 6.6 ± 1.3 nm of MNPs 40. For both the ferrite nanoparticles the calculated CV was of 20.2%.

These nanoparticles presented a very high colloidal stability even after 1 year of storage at room temperature. As shown in Fig. S3,† the DLS analysis of MNPs 29 and MNPs 40 resulted in

Table 4 Saturation magnetization (M_s), remanent magnetization (M_r) and coercive field (H_c) values measured at 298 K and 5 K for Zn/Mn FNP samples

Sample	T = 298 K			T = 5 K		
	M_s (Am^2 kg^{-1})	M_r (Am^2 kg^{-1})	H_c (kA m^{-1})	M_s (Am^2 kg^{-1})	M_r (Am^2 kg^{-1})	H_c (kA m^{-1})
MNPs 32	107.5	6.0	5.1	127.7	33.1	20.1
MNPs 33	40.3	0.3	1.6	56.6	12.6	35.1
MNPs 34	73.0	2.6	2.6	96.3	19.8	23.5
MNPs 35	71.4	2.7	2.7	90.7	23.3	15.5
MNPs 36	67.9	2.0	2.0	98.9	23.1	16.0
MNPs 37	66.1	2.1	2.1	90.3	26.4	18.1
MNPs 38	55.8	0.9	1.5	79.4	23.2	27.0

Table 5 Summary of each type of nanoparticle synthesized at different time intervals of crystal growth and their characteristics

Sample	Crystal growth	[Fe] (mM)	DLS size (nm)	PDI
MNPs 39	90 s	469.6	32.16	0.292
MNPs 40	**120 s**	**288.3**	**43.02**	**0.114**
MNPs 41	300 s	319	44.75	0.355
MNPs 36$_{DX}$	3 hours	1449	48.59	0.144

All the reported analyses referred to dextran-coated nanoparticles.
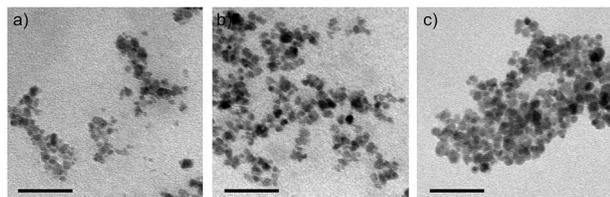
Fig. 6 TEM images of Zn/Mn FNPs obtained with crystal growth steps of 90″ (MNPs 39, panel a), 120″ (MNPs 40, panel b) and 300″ (MNPs 41, panel c). All scale bars correspond to 50 nm.
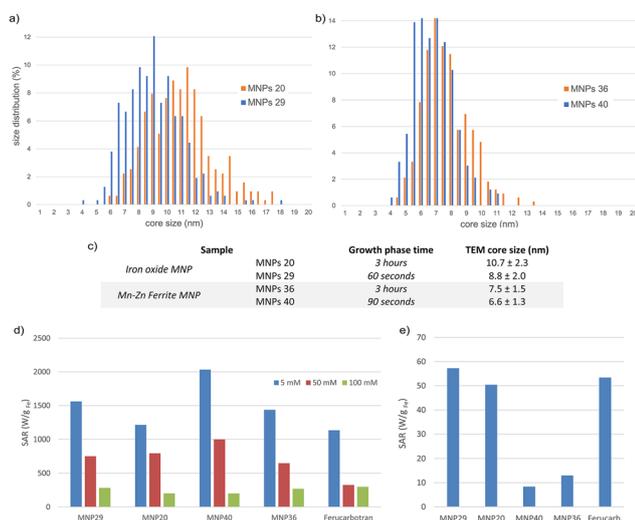
Fig. 7 Statistical analysis (a–c) of the TEM core size of iron oxide MNPs 20 and 29 (a) and Zn/Mn ferrite MNPs 36 and 40 (b). For each sample at least 300 particles and three different batches have been considered. Heating properties of selected MNPs in aqueous dispersion (d and e). SAR values (expressed in W g$_{Fe}$$^{-1}$) were recorded for photothermia (panel d, 808 nm laser – 1.6 W cm^{-2}) and for magnetic hyperthermia (panel e, 471 kHz – 18 mT).

similar profiles, with negligible variations (around 10%) in size and PDI.

To evaluate the heating potential of the synthesized nanoparticles, two approaches were explored: photothermia and magnetic hyperthermia. For both techniques, the heat-generating capacity of the nanoparticles (specific absorption rate, W g$_{Fe}$$^{-1}$) was normalized by the MNP iron concentration. For photothermia, the heating performances decreased with increasing concentration of nanoparticles in the suspension,

as previously reported.[33] Both formulations based on iron oxide (MNPs 20 and 29) show higher SAR values than the Ferucarbotran® used as a standard. Even higher values were obtained with the MNPs 36 and 40 Zn/Mn FNPs (Fig. 7d). Interestingly, both samples obtained with the fast growth method, MNPs 29 and 40, proved to be more efficient than the equivalents obtained with the traditional growth technique (MNPs 20 and 36), confirming the effectiveness of the method used. Regarding magnetic hyperthermia (Fig. 7e), the iron oxide nanoparticles showed performances comparable with the Ferubarbotran® standard. In contrast, the Zn/Mn FNPs did not produce satisfactory results in terms of SAR and therefore were not suitable for the application of this protocol.

3.9 Loading of MNPs into red blood cells

In this work various nanoparticulate formulations, obtained with different synthesis protocols, and their possible suitability for encapsulation in the human red blood cells (RBCs), have been reported with the aim to obtain new superparamagnetic constructs potentially useful in MRI and/or magnetic particle imaging (MPI).

The first chemical syntheses have led to different new nanoparticle suspensions (MNPs) composed of iron oxides and/or ferrites containing manganese and zinc with different physico-chemical characteristics. All nanoparticle suspensions were tested for encapsulation in the human red blood cells (RBCs) using a hypotonic dialysis method.[21] An automated hemocytometer has been used to assess biological parameters of MNP-loaded RBCs obtained at the end of the loading procedure, in comparison with control cells, Table 6. The final recovery of these MNP-RBC constructs, expressed as the percentage of cells obtained with respect to those utilized during the dialysis step, was also calculated. Table 6 shows also the values of longitudinal (T1) and transverse (T2) relaxation times obtained by NMR measurements of all MNP-RBC-loaded samples.

Despite the data shown in Table 6 demonstrating a significant decrease in T1 and T2 values of RBCs-MNPs compared to the values of control samples (ND, not dialyzed RBCs; 2210 ms, and UL, unloaded RBCs, 2080 ms), TEM analyses have shown that these nanoparticle formulations are not suitable for encapsulation in the human red blood cells (Fig. 8).

In fact, representative samples such as MNPs 36$_{CIT-filt\ 0.22}$ RBCs (Fig. 8a), MNPs 20$_{DX-non\ filt}$-RBCs (Fig. 8b), and MNPs 20$_{CHIT\ no\ filt}$-RBCs (Fig. 8c) reveal the presence of abundant iron oxides only in the extracellular spaces. Therefore, despite a strong decrease of T1 and T2 values being evidenced (Table 6) which would indicate the presence of iron oxide amounts (even higher for some samples) in the human RBC samples, the nanomaterials were not really encapsulated.

Moreover, it appears that chitosan is the least suitable coating agent to permit the encapsulation of nanoparticles in the RBCs.

In fact, the use of MNPs 20$_{CHI-non\ filt}$ leads to complete cell lysis (and this also when low iron amounts such as 2.8 mg mL^{-1} RBCs 70% are used, data not shown) evidencing that not all surfactant agents are eligible to preserve the biocompatibil-

Table 6 First superparamagnetic nanoparticle suspensions tested for encapsulation in human red blood cells

Samples	Metal ions	Coating	$T1$ (ms)	$T2$ (ms)	MCV (fl)	MCH (pg)	MCHC (g dl^{-1})	Cell recovery (%)
ND-RBCs	—	—	2210	63	88	31	34.3	—
UL-RBCs	—	—	2080	63	76	22.2	29.1	70
MNPs $11_{CIT-filt.0.22}$-RBCs	Fe	Citrate	40.9	<5	67	51.9	77.9	48
MNPs $14_{DX-non\ filt.}$-RBCs	Fe	Dextran	490	4.9	82	26.4	32.2	49
MNPs $20_{DX-non\ filt.}$-RBCs	Fe	Dextran	93.4	12.6	69	25.3	36.4	48
MNPs $20_{CHI-non\ filt.}$-RBCs	Fe	Chitosan	—	—	84	9.9	11.9	0
MNPs $35_{CIT-filt.0.22}$-RBCs	Fe/Mn/Zn	Citrate	—	—	76	10.7	14	21
MNPs $36_{CIT-filt.0.22}$-RBCs	Fe/Mn/Zn	Citrate	23.7	10.7	63	19.9	31.3	39

MNP–RBC loaded samples were prepared by using 11.2 mg Fe of each colloidal suspension added to 1 mL of RBCs at 70% of hematocrit during the dialysis step of the loading procedure. Values were compared to those of control cells (ND-RBCs; not dialysed RBCs and UL-RBCs; unloaded-RBCs).
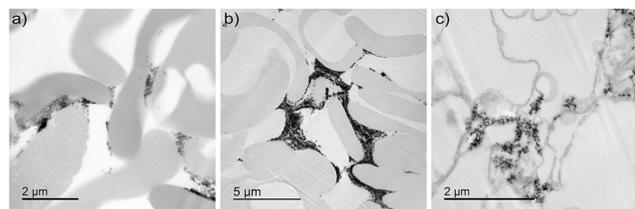

Fig. 8 Representative TEM images of some RBC samples obtained at the end of the loading procedure, by using three different nanoparticle types, with different surface coatings, such as (a) MNPs 36_{CIT} (citrate coated nanoparticles), (b) MNPs $20_{DX-non\ filt}$ (dextran coated nanoparticles), and (c) MNPs 20_{CHIT} (chitosan coated nanoparticles).

ity of the nanoparticle formulation (Table 6 and Fig. 8). Furthermore, the final cell recovery of MNP-loaded RBC samples was significantly lower (ranging from 0 to 49%) compared to the control unloaded RBC sample (UL-RBCs, 70%). The data obtained with the first nanoparticle formulations allowed us to understand how to modify the chemical synthesis protocol, which also depends on the ability of nanomaterials to be more efficiently encapsulated in the RBCs.

In a second step, other nanoparticle suspensions were synthesized according to the nucleation time and multiple-fil-

trations (as reported in sections 3.4 and 3.5) in order to improve their ability to be loaded in the erythrocytes. Table 7 shows some biological parameters (such as MCV, MCH, and MCHC) and $T1$ and $T2$ values obtained by NMR measurements of these MNP-RBC-loaded samples.

The MNP-loaded RBC samples present a cell volume similar to control cells (ND- and UL-RBCs) except for MNPs $26_{DX-non\ filt.}$-RBC and MNPs $25_{DX-filt.0.22}$-RBC samples that are much smaller (MCV; 52 and 56 fl, respectively). Moreover, these two last samples have less mean hemoglobin concentration (MCH) than the other MNP-loaded samples. All samples have lower cell recovery (ranging from 43 to 67%) with respect to the control sample (UL-RBCs; 70%) at the end of the procedure.

TEM analyses (Fig. 9) permitted us to establish which nanomaterials are more suitable for their encapsulation in the erythrocytes as not in all cases a strong decrease of $T1$ and $T2$ values corresponded to the effective entrapment of iron oxide into cells.

Particularly, MNP$35_{DX-filt.0.22}$-RBCs (Fig. 9a) and MNP$36_{DX-filt.0.1}$-RBCs (Fig. 9b) showed the presence of iron oxides; however, MNP$36_{DX-filt.0.1}$-RBCs evidenced the iron oxide nanomaterial in monodisperse form and only into cells, while in the MNP$35_{DX-filt.0.22}$-RBC sample, iron oxide clusters were found both in the cells and in the extracellular space.

Table 7 MNP-loaded RBC samples obtained by using nanoparticles synthesized by varying the nucleation time and multiple-filtrations (as reported in Materials and methods)

Samples	$T1$ (ms)	$T2$ (ms)	MCV (fl)	MCH (pg)	MCHC (g dl^{-1})	Cell recovery (%)
ND-RBCs	2236	57.7	88	29.3	33.4	—
UL-RBCs	2192	54.5	75	22.6	31.3	70
MNPs $26_{DX-non\ filt.}$-RBCs	836.5	5.3	52	13.4	25.6	67
MNPs $25_{DX-filt.0.22}$-RBCs	452.4	<5	56	13.6	24.2	53
MNPs $20_{DX-filt.0.22}$-RBCs	541.7	<5	68	20	29.3	50
MNPs $36_{DX-filt.0.22}$-RBCs	414.6	8.3	75	19.6	26.1	43
MNPs $35_{DX-non\ filt.}$-RBCs	556.4	10.3	74	15.1	20.4	44
MNPs $35_{DX-filt.0.22}$-RBCs	503.8	8.8	81	22.8	28.2	48
MNPs $20_{DX-filt.0.1}$-RBCs	**664.4**	**<5**	**67**	**18.7**	**27.8**	**61**
MNPs $36_{DX-filt.0.1}$-RBCs	**652**	**11.7**	**83**	**21.9**	**26.3**	**60**

Samples were characterized by $T1$ and $T2$ NMR measurements and evaluation of some biological properties (ND-RBCs; not dialysed RBCs and UL-RBCs; unloaded-RBCs; MNP-loaded RBCs were prepared using 11.2 mg Fe per mL of RBCs 70% Ht).
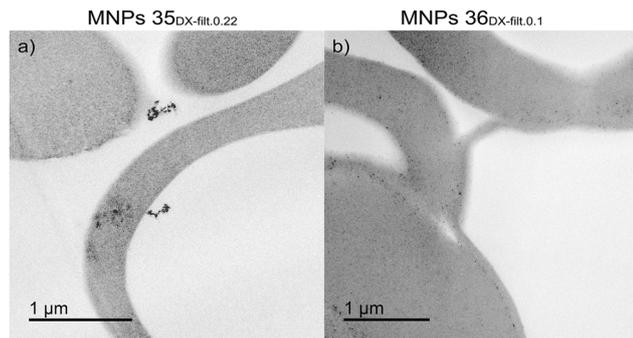
MNPs 35$_{DX-filt.0.22}$

MNPs 36$_{DX-filt.0.1}$

Fig. 9 TEM images of slices of human RBCs loaded with (a) MNPs 35$_{DX-filt.0.22}$ and (b) MNPs 36$_{DX-filt.0.1}$. Additional TEM images concerning the effect of filtration on sample MNPs 20 are reported in Fig. S4.†

It appears that magnetic nanoparticles processed with 0.1 μm filters, such as MNPs 20$_{DX-filt.0.1}$ and MNPs 36$_{DX-filt.0.1}$, have enabled achieving cell recoveries (60–65%) similar to those of control cells (UL-RBCs) at the end of the loading procedure (Table 7). However, the results showed that the MNPs 36$_{DX-filt.0.1}$ nanoparticle suspension appears the most eligible among the nanoparticle formulations using the 0.1 μm filter to maintain the native properties of RBCs at the end of the loading procedure.

Concerning the formulations processed with the 0.22 μm filter, a higher decrease of $T1$ and $T2$ values was observed (for example for MNPs 25$_{DX-filt.0.22}$ and MNPs 36$_{DX-filt.0.22}$ samples, Table 7), but lower final cell recovery of loaded RBCs was found (43–53%).

Afterwards, the nanoparticles obtained with a very short growth phase (see section 3.6 above) were tested for the loading procedure with human RBCs and the results are reported in Table 8. It appears that a growth phase of 0.5–5 minutes during the synthesis process of nanoparticles, in combination with 0.1 μm filtration, and providing formulations such as MNPs 41 lead to nanoparticle formulations (both iron oxide-MNPs and ferrite-MNPs) with greater ability to be encapsulated in the RBCs (Fig. 10). However, not all these nanoparticle formulations are very efficiently encapsulated (Fig. 10), despite a remarkable decrease of $T1$ and $T2$

values (*e.g.* for MNPs 28$_{DX-filt 0.1}$, MNPs 30$_{DX-filt 0.1}$ and MNPs 39$_{DX-filt 0.1}$-loaded RBC samples) being evidenced.

Therefore, the chemical synthesis of nanoparticles with a very reduced growth phase (order of minutes) appears to lead to an improvement of encapsulation into cells, of both pure iron oxide formulations, such as MNPs 30$_{DX-filt 0.1}$, and specific ferrite formulations such as MNPs 41 nanoparticle suspension, although, in some cases, the MNP-loaded RBC samples still present some iron clusters outside of cells (Fig. 10d).

TEM analyses have permitted us to continue the experiments with selected best type of nanoparticle, namely iron oxide-MNPs 29$_{DX-filt 0.1}$ and ferrite-MNPs 40$_{DX-filt 0.1}$. These specific nanoparticles are efficiently encapsulable in the human RBCs; both magnetic nanoparticle suspensions are present inside the cells and also evenly distributed in the cytoplasm and, moreover, in the MNPs 29- and MNPs 40-loaded RBC samples there are no iron oxides adhering to the cell surface or in the extracellular spaces (Fig. 11c and d for MNPs 29$_{DX-filt 0.1}$ and e and f for MNPs 40$_{DX-filt 0.1}$).

Moreover, MNPs 29 and MNPs 40-loaded RBC samples maintain the native cell morphology when compared to control samples (UL-RBCs, Fig. 11a and b). Electron microscopy analyses validate the iron concentration (mM) obtained from NMR measurements and by using calibration curves for MNPs 29 and MNPs 40 nanoparticles, respectively. The remarkable decrease of $T1$ and $T2$ values (*e.g.* $T1$ for MNPs 29-loaded RBCs, 394.3 ms; $T1$ for MNPs 40-loaded RBCs, 141.9 ms, Table 8) with respect to the control value (UL-RBCs, 2135 ms) corresponds to effective entrapment of iron oxides in the cells. The calibration curves for MNPs 29 and MNPs 40 nanoparticles were recorded using RBC suspensions at 44% of hematocrit. The values of $1/T1c–1/T10$ and of $1/T2c–1/T20$ have been used to obtain the values of longitudinal and transverse relaxivities ($r1 = 1.1379$ and $r2 = 180.02$, respectively, for MNPs 29 and $r1 = 2.5176$ and $r2 = 97.643$, respectively, for MNPs 40 (Fig. 12)). Essentially, calibration curves were obtained as reported in the ESI for the Ferucarbotran® contrast agent (Fig. S5†). By using $r1$ values, the amounts of iron present in the MNPs 29- and MNPs 40-loaded RBC samples were calculated; mM Fe concentrations, obtained by using a range of 2.8–22.4 mg Fe per mL RBCs 70% during the loading procedure, are reported in Table 9. The data show that the

Table 8 Characterization of L3-MNP-RBC constructs obtained with MNPs dextran-coated and processed with 0.1 μm filters

Samples	$T1$ (ms)	$T2$ (ms)	Fe [mM]	MCV (fl)	MCH (pg)	MCHC (g dl^{-1})	Cell recovery (%)
UL-RBCs	2135	67.5	—	75	22	29.2	70
MNPs 28$_{DX-filt 0.1}$-RBCs	150	6.7	4.75	72	44.3	61.3	56
MNPs 29$_{DX-filt 0.1}$-RBCs	**394.3**	**<5**	**1.87**	**70**	**19.5**	**27.9**	**60**
MNPs 30$_{DX-filt 0.1}$-RBCs	532.2	<5	1.1	78	19.8	25.4	51
MNPs 31$_{DX-filt 0.1}$-RBCs	726	5.2	0.71	82	22.5	27.5	49
MNPs 39$_{DX-filt 0.1}$-RBCs	351.6	5.4	1.82	68	12.3	18.2	59
MNPs 40$_{DX-filt 0.1}$-RBCs	**141.9**	**<5**	**2.66**	**75**	**19**	**25.6**	**47**
MNPs 41$_{DX-filt 0.1}$-RBCs	297.9	<5	2.2	76	16.4	21.5	52

The samples were prepared by using 11.2 mg Fe per mL RBCs at 70% of hematocrit. Results were compared to those of unloaded RBCs (UL-RBCs) obtained by the same procedure with the exception that they were dialysed in the absence of the magnetic material.
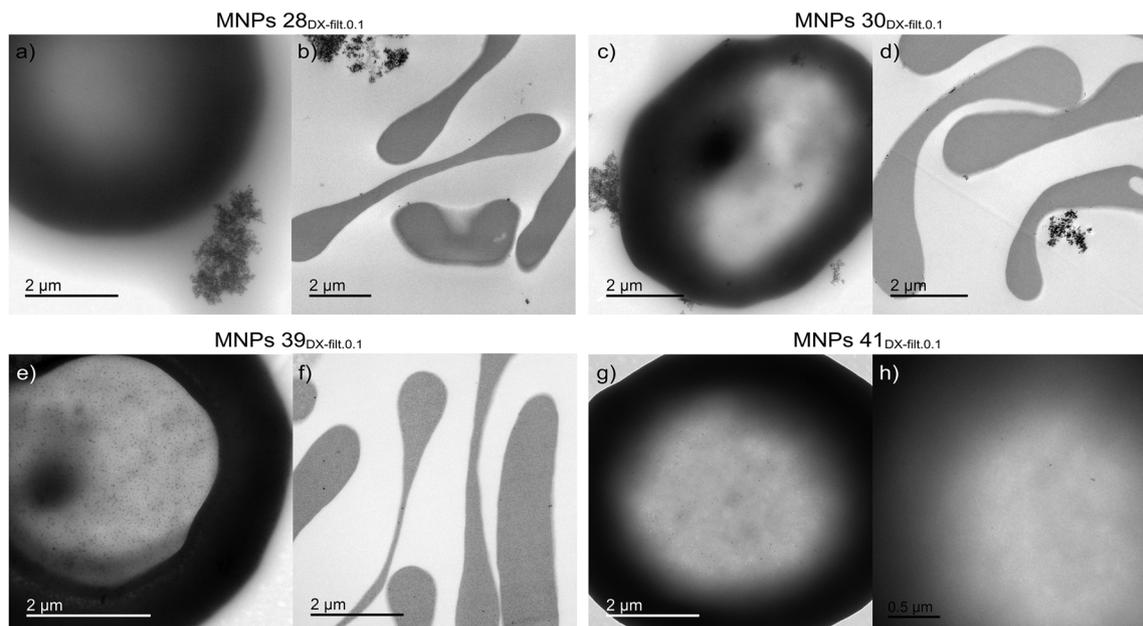
MNPs 28$_{DX-filt.0.1}$ MNPs 30$_{DX-filt.0.1}$

MNPs 39$_{DX-filt.0.1}$ MNPs 41$_{DX-filt.0.1}$

Fig. 10 TEM images of human RBCs loaded with MNPs 28$_{DX-filt\ 0.1}$ (a and b), MNPs 30$_{DX-filt\ 0.1}$ (c and d), MNPs 39$_{DX-filt\ 0.1}$ (e and f) and MNPs 41$_{DX-filt\ 0.1}$ (g and h). Images in a, c, e, g and h represent whole-RBC analyses, whereas images in b, d and f were obtained from slices of MNP-loaded-RBCs.

efficiency of iron encapsulation for both nanomaterials increases with the increased iron amounts used; an encapsulation of iron ranging from 0.6 ± 0.1 to 1.9 ± 0.4 mM Fe for MNPs 29-loaded RBCs and from 0.5 ± 0.1 to 2.8 ± 0.1 mM Fe for and MNPs 40-RBCs was obtained. Moreover, the data have indicated that the cell morphology and biological properties of the MNPs 29- and MNPs 40-loaded RBCs are not significantly different from those of native cells (Table 9). Only at higher iron amounts used for the loading procedure a slight decrease of MCH and MCHC values occurs. These preliminary experiments have evidenced the suitability of iron oxide-MNPs 29 and ferrite-MNPs 40 nanoparticles for encapsulation in human RBCs despite the final RBC-constructs showing different cell recovery values at the end of the loading procedure (MNPs 40-loaded RBCs lower than MNPs 29-loaded RBCs, Table 9).

On the other hand, the cell recovery of MNPs 29- and MNPs 40-loaded human RBCs obtained at the end of the procedure decreases when higher amounts (L4) of nanoparticles are used (from $62 \pm 2.8\%$ to $54.3 \pm 10.9\%$ for MNPs 29-RBCs and from $53.6 \pm 5.1\%$ to $42 \pm 1.4\%$ for MNPs 40-RBC samples, Table 9). TEM images showed iron oxides inside the cells evenly distributed in the cytoplasm of MNPs 29- and MNPs 40-loaded RBCs. However, in some cases, the presence of a few iron oxide clusters was also found in cells and particularly in MNPs 29-loaded RBCs (Fig. 11).The data obtained so far indicate that the ferrite MNPs 40 nanoparticles have a higher encapsulation efficiency (L4-MNPs 40-loaded RBC; 2.8 ± 0.1 mM Fe) than the iron oxide MNPs 29 nanoparticles (L4-MNPs 29-loaded RBCs 1.9 ± 0.4 mM Fe). However, it should be considered that the final cell recovery remarkably decreases. We also tested these nanomaterials with murine red blood cells in order to under-

stand if an *in vivo* application of these MNP-loaded RBC constructs can be considered. Table S4† and Table 10 report representative MNPs 29- and MNPs 40-loaded RBCs obtained by using human and murine red blood cells and 11.2 mg Fe per mL RBCs 70% (to obtain L3-loaded samples), respectively. The data obtained at the end of the loading procedure have indicated that typical biological properties of murine RBCs were maintained (Table 10). The cell recovery of murine RBCs at the end of the loading procedure appears similar for MNPs 29- and MNPs 40-RBC constructs ($34.3 \pm 8.1\%$ and $32.3 \pm 6.7\%$, respectively) and both values are slightly lower than the values obtained for the control sample ($44.2 \pm 5.4\%$ for the UL-RBCs).

As expected, murine RBCs are smaller in diameter, size and volume and permit encapsulation of lower MNP amounts into human RBCs; on the other hand, they are more fragile and the cell recovery at the end of the procedure is lower with respect to that obtained by using human RBCs.

However, the *in vitro* results with murine RBCs reported in Table 10 are essential to evaluate the possibility to perform *in vivo* experiments. The murine model permits us to study the survival in the blood circulation of these new MNP-RBC constructs in forthcoming *in vivo* studies on best-performing MNP-RBC constructs.

The decrease of $T1$ and $T2$ values, obtained by the NMR measurements, indicated a possible encapsulation of these nanomaterials also in murine RBCs. By using the calibration curves (Fig. 13), specifically obtained for MNPs 29 and MNPs 40 nanoparticles, it was possible to calculate mM Fe concentrations present in MNPs 29- and MNPs 40-loaded samples (Table 10). The resulting mM iron concentrations entrapped in murine MNPs 29- and MNPs 40-loaded RBCs, calculated using
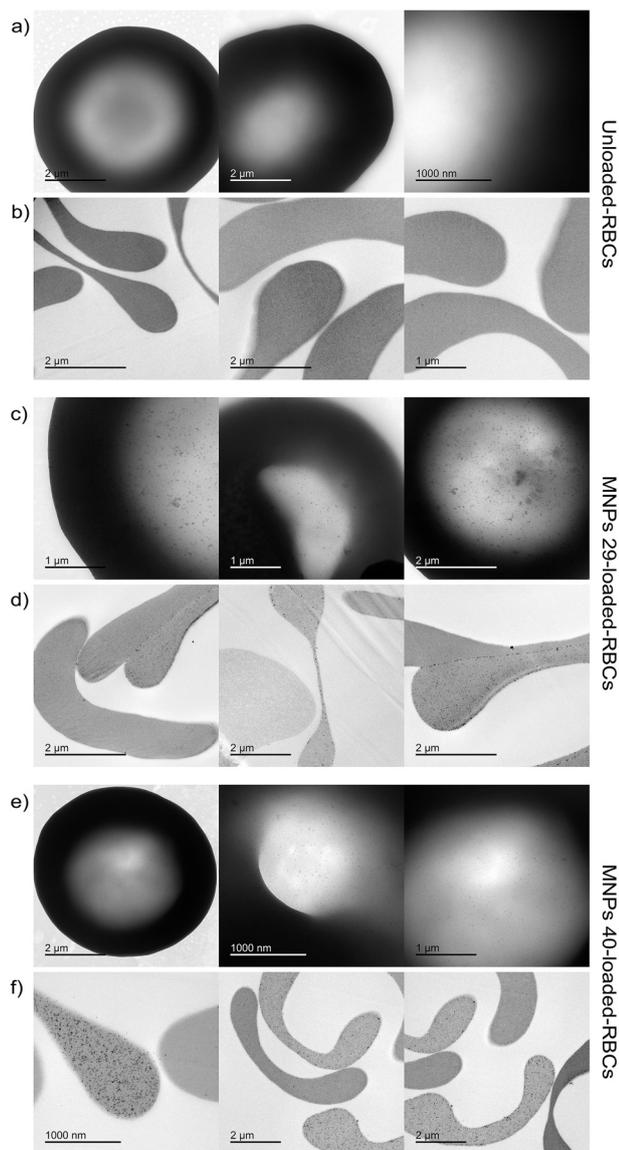
Fig. 11 TEM images of RBCs (whole cells in a, c, and e; slices in b, d, and f) obtained at the end of the loading procedure by using MNPs $29_{DX-filt\ 0.1}$ (c and d) and MNPs $40_{DX-filt\ 0.1}$ (e and f) nanoparticles. Unloaded-RBCs are reported in panels (a) and (b). TEM images of non-dialyzed RBCs (ND-RBCs) are shown in Fig. S6.†

Fig. 12 NMR dose−response curves generated by adding known amounts of MNPs $29_{DX-filt\ 0.1}$ nanoparticles (A and B) or MNPs $40_{DX-filt\ 0.1}$ nanoparticles (C and D) to human RBCs at 44% Ht. The values of $1/T1c−1/T1_0$ and of $1/T2c−1/T2_0$ have been used to obtain the values of longitudinal relaxivity $r1 = 1.1379$ (A) and transverse relaxivity $r2 = 180.02$ (B) for MNPs 29 and $r1 = 2.5176$ (C) and $r2 = 97.643$ (D) for MNPs 40.

The MPS signal was acquired upon application of a sinusoidal magnetic field as reported in the Experimental section. The MPS results of free MNPs and MNP-loaded RBCs were verified against the measurement of unloaded RBCs as well as an empty signal measurements, which mimic the noise level of the MPS. Thus, the results are valid up to the frequency at which their responses cross the response of the empty reference signal. In order to investigate the difference between the RBC signal and the signal of the immobilized particles, the spectral responses are normalized to the immobilized signal. The results for the MNPs 29- and the MNPs 40 particles are shown in Fig. 15. MNPs 29-loaded RBCs give a frequency signal which is slightly weaker than the signal of their immobilized counterparts, by approximately half an order of magnitude. The two signals run in a parallel manner along the higher harmonics, up to a frequency of 750 kHz, at which the signals start to vanish in the noise. This shows that the RBC signal is very close to the signal of immobilized MNPs 29 and differs only by a frequency constant scaling factor (Fig. 15a). For the MNPs 40-loaded RBCs the measurements show a similar result (Fig. 15b).

Moreover, the MPS signal runs parallel to the signal of the immobilized MNPs 40 particles over the first higher harmonics. As of 400 kHz, the signal starts to fluctuate more compared to the signal of the immobilized particles. Interestingly, the free particle signal shows the same fluctuation. Again, the measurements start to vanish in the noise at approximately 750 kHz. Therefore, it appears that MNPs 29-RBC constructs perform slightly better than MNPs 40-RBCs when evaluated with MPS.

Finally, to investigate the potential of the MNPs-RBC constructs as MRI contrast agents, free-MNPs and MNPs-RBCs were dispersed in agarose and analyzed using the T_2-MSME sequence. For MNPs 29, the obtained R_2 was 405 mM^{-1} s^{-1}, which is very high when compared to reported values in the literature. Once loaded into RBCs, the R_2 of these nanoparticles

$r1$ values derived from calibration curves, were $1.90 ± 0.02$ mM and $0.90 ± 0.20$ mM, respectively, for MNPs 29- and MNPs 40-RBC constructs. It is evident that the encapsulation of the Ferucarbotran® contrast agent (gold standard) was more efficient when both human and murine RBCs were used (Table 10 and Table S4†).

Anyway, these preliminary studies have indicated that the iron oxide nanoparticles such as MNPs 29 and ferrite-MNPs 40 nanoparticles, are also encapsulable in the murine RBCs (Fig. 14). These data are promising to continue the validation of these nanomaterials for the loading in the murine erythrocytes with the aim to perform future *in vivo* experiments through the use of a murine animal model.
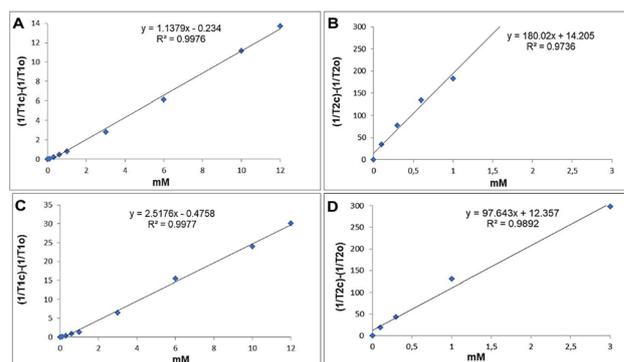
Table 9 Characterization of the constructs MNPs $29_{\text{DX-filt 0.1}}$- and MNPs $40_{\text{DX-filt 0.1}}$-loaded human RBCs. Samples were obtained after the loading procedure performed with different iron amounts (from 2.8 to 22.4 mg Fe per mL RBCs 70%)

Samples	$T1$ (ms)	$T2$ (ms)	Fe [mM]	MCV (fl)	MCH (pg)	MCHC (g dl^{-1})	Cell recovery (%)
UL-RBCs	2069 ± 15.6	62.1 ± 1.3	—	77.5 ± 0.7	25.2 ± 0.6	34.3 ± 1.3	70.1 ± 0.1
L1-MNPs $29_{\text{DX-filt 0.1}}$	939 ± 270	6.9 ± 0.9	0.6 ± 0.1	74 ± 4.2	25.4 ± 0.3	35.2 ± 1.5	62 ± 2.8
L2-MNPs $29_{\text{DX-filt 0.1}}$	733 ± 173	6 ± 0.5	1 ± 0.3	74 ± 0.7	25 ± 0.6	34 ± 0.8	57 ± 12
L3-MNPs $29_{\text{DX-filt 0.1}}$	481.5 ± 123	<5	1.5 ± 0.5	74 ± 5.7	21.8 ± 3.2	29.4 ± 2.1	54.9 ± 7.3
L4-MNPs $29_{\text{DX-filt 0.1}}$	402.5 ± 70.2	<5	1.9 ± 0.4	70.5 ± 6.4	20.3 ± 3.6	28.6 ± 2.5	54.3 ± 10.9
L1-MNPs $40_{\text{DX-filt 0.1}}$	590 ± 64.1	9.3 ± 0.4	0.5 ± 0.1	76.5 ± 3.5	25.1 ± 0.3	33 ± 1.9	53.6 ± 5.1
L2-MNPs $40_{\text{DX-filt 0.1}}$	373.3 ± 42.5	5.7 ± 0.4	0.9 ± 0.1	75.5 ± 0.7	24.7 ± 0.8	32.8 ± 0.8	52.2 ± 5.9
L3-MNPs $40_{\text{DX-filt 0.1}}$	196.5 ± 77.2	<5	2 ± 0.9	74.5 ± 0.7	21.4 ± 3.3	28.6 ± 4.2	46.5 ± 0.7
L4-MNPs $40_{\text{DX-filt 0.1}}$	135 ± 5.2	<5	2.8 ± 0.1	74.5 ± 2.1	18.9 ± 1.1	25.3 ± 2.5	42 ± 1.4

Table 10 Data obtained after the loading of MNPs $29_{\text{DX-filt 0.1}}$ and MNPs $40_{\text{DX-filt 0.1}}$ nanoparticles with murine RBCs

Samples	$T1$ (ms)	$T2$ (ms)	Fe [mM]	MCV (fl)	MCH (pg)	MCHC (g dl^{-1})	Cell recovery (%)
UL-RBCs	2078.5 ± 108	57.4 ± 4.8	—	41.5 ± 0.7	15.9 ± 0.6	38.5 ± 1.9	44.2 ± 5.4
L3-MNPs 29	484.4 ± 26.8	5.9 ± 2.1	1.90 ± 0.02	41.5 ± 0.7	14.9 ± 0.6	35.6 ± 0.9	34.3 ± 8.1
L3-MNPs 40	440.9 ± 92.3	7.8 ± 2.7	0.90 ± 0.20	41.0 ± 2.8	13.8 ± 1.3	33.8 ± 0.9	32.3 ± 6.7
L3-Ferucarbotran	177 ± 27.60	<5	4.05 ± 0.83	40 ± 0.7	11.75 ± 1.06	31.5 ± 0.8	43 ± 8.3

Samples obtained by using 11.2 mg Fe per mL RBC70%. Values are expressed as means ± SD of three similar experiments.
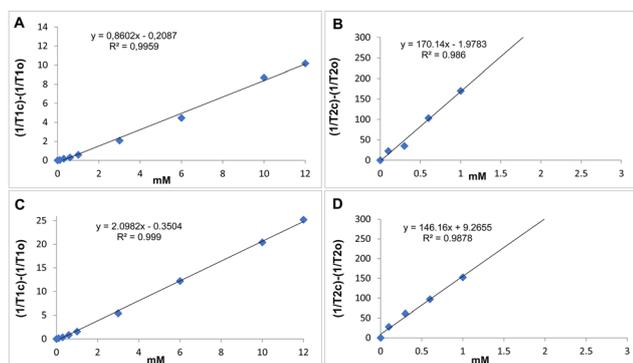

Fig. 13 NMR dose−response curves generated by adding known amounts of MNPs $29_{\text{DX-filt 0.1}}$ nanoparticles (A and B) or MNPs $40_{\text{DX-filt 0.1}}$ nanoparticles (C and D) to murine RBCs at 44% Ht. The values of $1/T1_{\text{c}} - 1/T1_0$ and of $1/T2_{\text{c}} - 1/T2_0$ have been used to obtain the values of longitudinal relaxivity $r1 = 0.8602$ (A) and transverse relaxivity $r2 = 170.14$ (B) for MNPs 29 and $r1 = 2.0982$ (C) and $r2 = 146.16$ (D) for MNPs 40.

Fig. 14 TEM images of whole-murine RBCs obtained at the end of the loading procedure by using Ferucarbotran (a and b), MNPs $29_{\text{DX-filt 0.1}}$ (c and d) and MNPs $40_{\text{DX-filt 0.1}}$ (e and f) nanoparticles. Additional TEM images of Ferucarbotran-loaded human RBCs are reported in Fig. S7.†

decayed 10-fold, with a value of 40 mM^{-1} s^{-1}. Concerning the MNPs 40, the measured R_2 was lower than those of the corresponding iron oxide nanoparticles, with a value of 260 mM^{-1} s^{-1}. Anyway, the encapsulation in RBCs did not affect drastically the R_2 value, with a 2.3-fold decay at 110 mM^{-1} s^{-1}. The different behavior is representative of the different encapsulation of these two MNPs, whereas the MNPs 29 tended to produce small aggregates in the RBCs, and the smaller MNPs 40 nanoparticles were found to be more individually dispersed in the cell cytoplasm, as evidenced in Fig. 11.
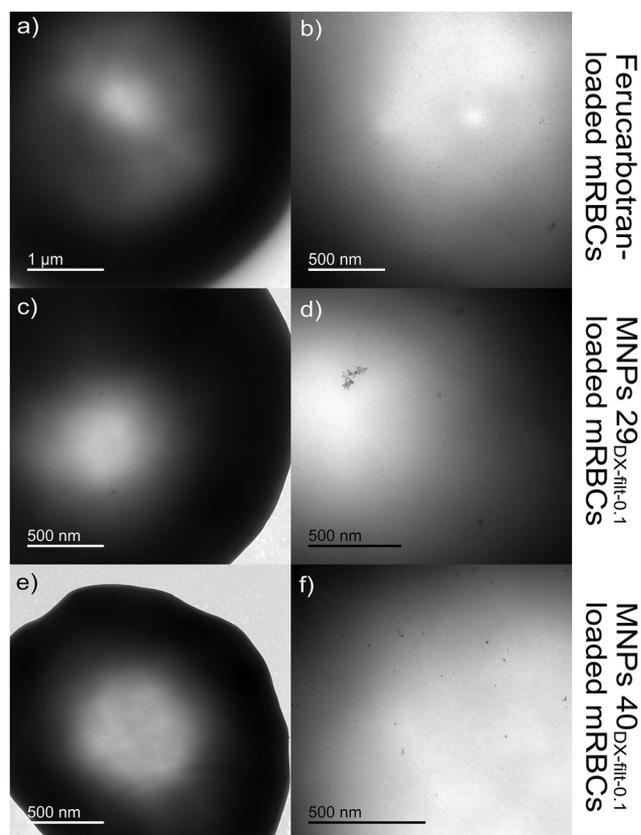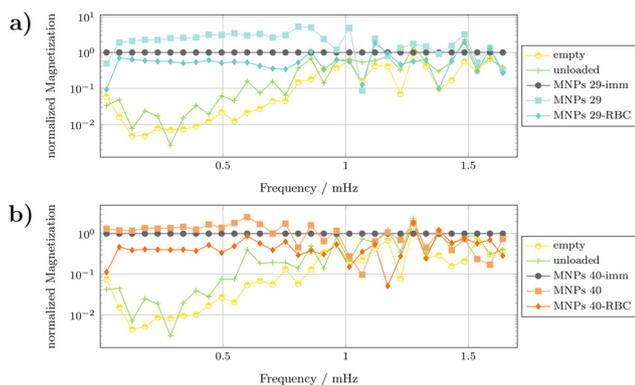
Fig. 15 MPS spectra of representative human L3-MNPs $29_{DX-filt\ 0.1}$-RBCs (a) and L3-MNPs $40_{DX-filt\ 0.1}$-RBCs (b) samples in comparison with the respective immobilized and liquid nanoparticles.

4. Conclusions

The production of new biomimetic contrast agents, like MNP-loaded RBCs, able to prolong the half-life of iron oxide based-contrast agents (CAs) is necessary in the field of diagnostic applications since radiologists need tracers with higher survival in the circulatory system in order to monitor patients over several days. This is particularly important for patients with pathologies (*e.g.* cardiovascular or brain diseases) to avoid repeated injection of the contrast agent. Medical imaging plays a central role in the global healthcare system, and the use of intravascular CAs continues to increase since their use improves patient diagnosis. A highly efficient blood pool CA is urgently needed to gain more precise diagnostic details in clinical applications. However, the potential risks of intravascular administration of any CA must be weighed against the potential benefits. The interface between CAs and biological media is a key factor that may influence the *in vivo* behaviors of the agents. In most cases, the CAs rapidly extravasate from the vasculature or they are recognized by immune systems and accumulate in the liver and spleen, leading to uncontrollable distribution. CAs with long blood circulation time are needed to improve investigations of the vascular system, such as functional cardiac diagnosis, angiography, or a cardiac wall motion assessment. The strategy described here is the use of RBCs as carriers for intravascular CAs. RBCs can restrain or camouflage CAs, thus prolonging their circulation time and restricting their extravasation, which increases the time window for vascular imaging. Among the proposed carriers, RBCs are attractive owing to their unique characteristics, including their long half-life in the bloodstream, biocompatibility, and large internal capacity (~90 fL). Moreover, scientists have not reported any adverse events after intravenous injection of autologous CA/drug-loaded RBCs in humans and no allergic reactions were recorded during follow-up.[36] The use of autologous RBCs not only increases the CA blood retention time but also strongly reduces the risk of allergic or other immune reactions that could occur as well as adverse events in response to some

drugs for example. Encapsulation of CAs in RBCs for clinical use is currently in practice since technology that permits automatic loading is now available. In fact, two European companies, EryDel SpA in Italy (https://www.erydel.com) and Erythec Pharma in France (https://www.erytech.com), have implemented medical devices to encapsulate drugs and diagnostics in human RBCs at the industrial level. Several pilot studies have documented the advantages of RBCs when used as delivery systems of angiographic agents or nanoparticles to prevent their extravasation and/or macrophage recognition and removal.[37] We think that MNP-loaded RBCs could be efficient new contrast agents in a similar way especially since in Europe the Resovist (Ferucarbotran) contrast agent has been discontinued. Although significant progress has been made in the field of diagnostic imaging using some very sophisticated modalities, it is likely that further improvements will be made, especially in image quality. It is necessary to have close collaboration among experts in multiple disciplines, since collaboration among radiologists, physicists, computer scientists, and engineers is fundamental for progress in the development of new strategies and diagnostic modalities in medical imaging to optimize investigation of the vascular system.

The systematic study conducted on human and murine erythrocytes has allowed to highlight the peculiar aspects of the synthesis of magnetic nanoparticles for the engineering of these circulating cells. We proposed synthesis protocols to overcome the limitations of non-optimal material that mostly led to the presence of particles in aggregated forms on the extracellular surface at the end of the loading procedure, by developing more suitable nanomaterials. The first requirement definitely concerns the stability of the nanomaterials, which was found related to the dispersity and size of the particles, but also to the surface coating. In this case, a polysaccharidic coating, based on dextran, proved to be excellent in terms of stability and long-term storage. Secondly, MNPs must not affect RBC viability, permitting a cell recovery at the end of the loading procedure similar to that of control cells. Within the different synthetic parameters, filtrations and a fine control of the crystal growth time were the most impactful parameters for the resulting MNPs. It was evidenced that nanoparticles with a crystal growth time below two minutes showed the best encapsulation performance. Furthermore, following the popular strategy for tailoring the MNPs properties of introducing divalent ions such as manganese and zinc into the crystalline structure,[38] we showed that the obtained Zn/Mn FNPs exhibited a reduction in nanoparticles size, through a modification of the crystal lattice parameters of the partially doped-spinel structure.[39] Unfortunately, the introduction of zinc and manganese resulted in a reduced saturation magnetization (and therefore a reduced R_2 relaxivity) but, remarkably, this strategy further enhanced the loading of these ferrites into human red blood cells. Our study allowed to select those nanomaterials that are most suitable for loading into RBCs producing new biocompatible MNP-constructs particularly useful for the imaging of the circulatory system. This takes on even more

significance considering that commercial and efficient iron-based contrast agent such as Resovist® (still considered one of the gold standards for imaging techniques as MRI and MPI) is currently available only in Japan. In addition to that, the Gd-based paramagnetic contrast agents that are routinely used alternatively as standard *T*1-contrast agents for clinical MRI nowadays,[40] can be highly toxic leading in some cases to the possible risk of acute renal failure and accumulation in bones, liver and spleen. Recently, safety concerns were raised for this class of agents, since gadolinium chelates are deposited in the brain for months or years, with particularly alarming long-term effects for pediatric diagnostic.[41] In this context, the present study permitted to understand how to improve the properties of newly synthesized nanoparticle suspensions to obtain MNPs-RBCs which in the next future we propose to use for imaging with MRI/fMRI. The novelty of this research consists in the production of magnetic nanoparticles suitable for the encapsulation procedure within human and murine RBCs. We consider it as a very important result since not all magnetic nanoparticles (synthesized from other groups in the past) can be encapsulated in the RBCs; moreover, the MNP suspensions here presented are very stable over time (months) and maintain their monodispersed form in the suspensions (MNPs 29 and MNPs 40 also) without precipitation. In addition, the Fe molar concentrations reached resulted in an optimal range to perform the dialysis step with RBCs. This is important to avoid the decrease of the RBC hematocrit percentage which can lead to a lower final cell recovery and therefore a lower yield to be used *in vivo*. An *in vivo* study in mice involving the best-performing MNP-RBC has been already set. We could envisage that the preliminary pharmacokinetic results obtained with murine RBCs will lead to a prolongation of MNPs survival in the blood circulation. The absence of nanomaterial on the cell surface membrane (or in the extracellular space) will avoid the fast phagocytosis by RES in the liver of MNPs-loaded-RBCs, as previously observed in *in vivo* analysis of Ferucarbotran-loaded RBCs.

Author contributions

R. Di Corato and A. Antonelli: conceptualization, methodology, investigation, validation, supervision, writing – review original draft, and editing. L. M. Slavu: methodology, investigation, data curation, and validation. E. S. Scarpa, P. Abdalla and N. Silvestri: data curation and investigation. C. Wilhelm, T. Pellegrino and K. Scheffler: methodology, writing – review, and editing. M. Magnani and R. Rinaldi: conceptualization, funding acquisition, writing – review, and editing. All authors have read and approved the final manuscript.

Conflicts of interest

There are no conflicts to declare.

References

1 P. Kucheryavy, J. B. He, V. T. John, P. Maharjan, L. Spinu, G. Z. Goloverda and V. L. Kolesnichenko, *Langmuir*, 2013, **29**, 710–716.

2 M. G. Lu, K. T. Al-Jamal, K. Kostarelos and J. Reineke, *ACS Nano*, 2010, **4**, 6303–6317.

3 R. K. Jain and T. Stylianopoulos, *Nat. Rev. Clin. Oncol.*, 2010, **7**, 653–664.

4 T. Ganz, *Microbiol. Spectrum*, 2016, **4**, 803–812.

5 A. Avasthi, C. Caro, E. Pozo-Torres, M. P. Leal and M. L. Garcia-Martin, *Top. Curr. Chem.*, 2020, **378**, 40.

6 J. M. Irache, I. Esparza, C. Gamazo, M. Agueros and S. Espuelas, *Vet. Parasitol.*, 2011, **180**, 47–71.

7 S. Vinogradov and X. Wei, *Nanomedicine*, 2012, **7**, 597–615.

8 V. Bhardwaj, A. Kaushik, Z. M. Khatib, M. Nair and A. J. McGoron, *Front. Pharmacol.*, 2019, **10**, 1369.

9 I. Cicha, C. Chauvierre, I. Texier, C. Cabella, J. M. Metselaar, J. Szebeni, L. Dezsi, C. Alexiou, F. Rouzet, G. Storm, E. Stroes, D. Bruce, N. MacRitchie, P. Maffia and D. Letourneur, *Cardiovasc. Res.*, 2018, **114**, 1714–1727.

10 Z. J. Zhou, L. J. Yang, J. H. Gao and X. Y. Chen, *Adv. Mater.*, 2019, **31**, 1804567.

11 H. Ittrich, K. Peldschus, N. Raabe, M. Kaul and G. Adam, *Rofo-Fortschritte Auf Dem Gebiet Der Rontgenstrahlen Und Der Bildgebenden Verfahren*, 2013, vol. 185, pp. 1149–1166.

12 Y. X. J. Wang, *Quant. Imaging Med. Surg.*, 2011, **1**, 35–40.

13 J. Rahmer, A. Antonelli, C. Sfara, B. Tiemann, B. Gleich, M. Magnani, J. Weizenecker and J. Borgert, *Phys. Med. Biol.*, 2013, **58**, 3965–3977.

14 F. Bossa, A. Latiano, L. Rossi, M. Magnani, O. Palmieri, B. Dallapiccola, S. Serafini, G. Damonte, E. De Santo, A. Andriulli and V. Annese, *Am. J. Gastroenterol.*, 2008, **103**, 2509–2516.

15 G. Mambrini, M. Mandolini, L. Rossi, F. Pierige, G. Capogrossi, P. Salvati, S. Serafini, L. Benatti and M. Magnani, *Int. J. Pharm.*, 2017, **517**, 175–184.

16 S. Serafini, L. Rossi, A. Antonelli, A. Fraternale, A. Cerasi, R. Crinelli, L. Chiarantini, G. F. Schiavano and M. Magnani, *Transfusion Medicine and Hemotherapy*, 2004, vol. 31, pp. 92–101.

17 R. Sabatino, A. Antonelli, S. Battistelli, R. Schwendener, M. Magnani and L. Rossi, *PLoS One*, 2014, **9**, e101260.

18 A. Antonelli, R. Crinelli, M. Bianchi, A. Cerasi, L. Gentilini, G. Serafini and M. Magnani, *Br. J. Haematol.*, 1999, **104**, 475–481.

19 A. Antonelli, C. Sfara, O. Weber, U. Pison, E. Manuali, S. Salamida and M. Magnani, *Nanomedicine*, 2016, **11**, 2781–2795.

20 A. Antonelli, C. Sfara and M. Magnani, *Nano Res.*, 2017, **10**, 731–766.

21 A. Antonelli, P. Szwargulski, E. S. Scarpa, F. Thieben, G. Cordula, G. Ambrosi, L. Guidi, P. Ludewig, T. Knopp and M. Magnani, *Nanomedicine*, 2020, **15**, 739–753.

22 F. J. Wei and Y. X. Duan, *Adv. Biosyst.*, 2019, **3**, 1800259.

23 P. Makvandi, M. L. Chen, R. Sartorius, A. Zarrabi, M. Ashrafizadeh, F. D. Moghaddam, J. Z. Ma, V. Mattoli and F. R. Tay, *Nano Today*, 2021, **40**, 101279.

24 J. W. M. Bulte, *Adv. Drug Delivery Rev.*, 2019, **138**, 293–301.

25 A. G. Roca, L. Gutierrez, H. Gavilan, M. E. F. Brollo, S. Veintemillas-Verdaguer and M. D. Morales, *Adv. Drug Delivery Rev.*, 2019, **138**, 68–104.

26 O. Veiseh, J. W. Gunn and M. Q. Zhang, *Adv. Drug Delivery Rev.*, 2010, **62**, 284–304.

27 R. Di Corato, A. Quarta, P. Piacenza, A. Ragusa, A. Figuerola, R. Buonsanti, R. Cingolani, L. Manna and T. Pellegrino, *J. Mater. Chem.*, 2008, **18**, 1991–1996.

28 J. P. Fortin, C. Wilhelm, J. Servais, C. Menager, J. C. Bacri and F. Gazeau, *J. Am. Chem. Soc.*, 2007, **129**, 2628–2635.

29 R. Massart, *IEEE Trans. Magn.*, 1981, **17**, 1247–1248.

30 K. Ludtke-Buzug, S. Biederer, T. Sattel, T. Knopp and T. M. Buzug, 4th European Conference of the International Federation for Medical and Biological Engineering (ECIFMBE), Antwerp, Belgium, 2008.

31 A. Antonelli, E. S. Scarpa, R. Di Corato, F. Thieben, C. Grüttner, T. Knopp and M. Magnani, *Int. J. Magn. Part. Imaging*, 2022, **8**, 2203038.

32 A. Espinosa, R. Di Corato, J. Kolosnjaj-Tabi, P. Flaud, T. Pellegrino and C. Wilhelm, *ACS Nano*, 2016, **10**, 2436–2446.

33 A. Espinosa, J. Kolosnjaj-Tabi, A. Abou-Hassan, A. P. Sangnier, A. Curcio, A. K. A. Silva, R. Di Corato, S. Neveu, T. Pellegrino, L. M. Liz-Marzan and C. Wilhelm, *Adv. Funct. Mater.*, 2018, **28**, 1803660.

34 M. C. Mascolo, Y. Pei and T. A. Ring, *Materials*, 2013, **6**, 5549–5567.

35 T. Saragi, B. L. Depi, S. Butarbutar, B. Permana and Risdiana, *J. Phys.: Conf. Ser.*, 2018, **1013**, 012190.

36 G. Caminiti, S. M. Carta, R. Flower, L. Rossi, M. Magnani, M. Fossarello and E. Peiretti, *Invest. Ophthalmol. Visual Sci.*, 2015, **56**, 3362.

37 A. Antonelli, S. Pacifico, C. Sfara, M. Tamma and M. Magnani, *Nanomedicine*, 2018, **13**, 675–687.

38 L. M. Slavu, R. Rinaldi and R. Di Corato, *Appl. Sci.*, 2021, **11**, 11183.

39 M. Porru, M. D. Morales, A. Gallo-Cordova, A. Espinosa, M. Moros, F. Brero, M. Mariani, A. Lascialfari and J. G. Ovejero, *Nanomaterials*, 2022, **12**, 3304.

40 D. P. J. Pan, A. H. Schmieder, S. A. Wickline and G. M. Lanza, *Tetrahedron*, 2011, **67**, 8431–8444.

41 H. E. Daldrup-Link, A. J. Theruvath, A. Rashidi, M. Iv, R. G. Majzner, S. L. Spunt, S. Goodman and M. Moseley, *Pediatr. Radiol.*, 2022, **52**, 354–366.